ChemSusChem

Research Article
doi.org/10.1002/cssc.202201088

Chemistry Europe
European Chemical Societies Publishing

www.chemsuschem.org

Electrolyte Engineering for Oxygen Evolution Reaction Over Non-Noble Metal Electrodes Achieving High Current Density in the Presence of Chloride Ion

Hiroki Komiya,[a] Tatsuya Shinagawa,[a] and Kazuhiro Takanabe*[a]

Direct seawater electrolysis potentially simplifies the electrolysis process and leads to a decrease in the cost of green hydrogen production. However, impurities present in the seawater, especially chloride ions (Cl^-), cause corrosion of the electrode material, and its oxidation competes with the anodic oxygen evolution reaction (OER). By carefully tuning electrode substrate and electrolyte solutions, the $CoFeO_xH_y$/Ti electrode with high double-layer capacitance actively and stably electro-catalyzed the OER in potassium borate solutions at pH 9.2 in the presence of 0.5 mol kg^{-1} Cl^-. The electrode possesses an active site motif composed of either a Co- or Fe-domain and benefits from an enlarged surface area. Selective OER was demonstrated in Cl^--containing electrolyte solutions at an elevated reaction temperature, stably achieving 500 mA cm^{-2} at a mere potential of 1.67 V vs. reversible hydrogen electrode (RHE) at 353 K for multiple on-off and long-term testing processes with a faradaic efficiency of unity toward the OER.

Introduction

Hydrogen (H_2) stands out as a promising energy carrier worldwide. Due to its characteristics of high energy density, flexibility in stored form, and no carbon dioxide emission when used, it can complement electricity generation. Water electrolysis driven by renewable energy processes that produce hydrogen serves as a green alternative technology to the current fossil-fuel-based ones. Critically, water electrolyzers operate with highly pure and/or alkaline water that feeds into the established commercial polymer electrolyte membrane (PEM) or alkaline water electrolyzer.[1,2] The use of the aqueous medium, such as the reactant feed, however, requires desalination and purification of the reactant water and contributes to H_2 cost-inefficiency.[3] Moreover, the recently recognized water crisis may hamper future large-scale deployment of water electrolyzers. Because of the increase in the global population growth and climate change,[4] no less than 80% of the world's population is facing difficulties in securing fresh and safe water.[5] In this context, seawater, which accounts for 97% of all water on Earth, has recently been regarded as a direct reactant of electrolyzers.[6]

Seawater electrolysis, however, faces several challenges caused by the impurities present in the seawater. For instance, on the cathode on which the hydrogen evolution reaction (HER) ideally would proceed, a metal hydroxide can precipitate during the operation, thus causing blockage and degradation of active sites on the cathode.[6] More specifically, because seawater has pH levels of 8.0 to 8.3[7] and does not contain buffering substances, the pH levels in the vicinity of the electrode shift to alkaline pH values as the HER proceeds. Cationic species present in the seawater, namely Ca^{2+} and Mg^{2+}, readily react with the locally generated hydroxide ions to form a solid hydroxide on the cathode.[8] One promising and likely solution to this issue is the addition of a buffering substance, which has been demonstrated to alleviate the fluctuation of the local pH level.[9] Another critical issue is caused by the chloride ions (Cl^-) present in the seawater. Although the anodic half-reaction of water electrolysis, namely the oxygen evolution reaction (OER), is thermodynamically preferable to the chloride oxidation reaction (COR), the relatively slow kinetics of the OER make these two reactions competitive. The consequence of the competitive process is the evolution of Cl_2 gas, hypochlorite (ClO^-), or both, both of which cause damage to both the instrument and the environment.[10,11]

Three main approaches for suppressing the COR have been reported. The first is the introduction of a Cl^- blocking layer that prohibits Cl^- from reaching the active site. Hashimoto and coworkers reported electrodes that consisted of an Mn-based mixed metal oxide covering an IrO_x active layer, which generated oxygen with a unity faradaic efficiency (FE) toward the OER (FE_{O_2}) and showed long-term stability under various Cl^--containing conditions.[12–14] They claimed that an OER mechanism originated from the active catalyst of MnO_x. On the other hand, Vos et al.[15] coated an OER-active IrO_x with a MnO_x film as a permselective membrane to repel Cl^-. The fabricated MnO_x/IrO_x electrode was previously demonstrated to selectively catalyze OER in the presence of Cl^- and achieve the FE

[a] H. Komiya, Dr. T. Shinagawa, Prof. K. Takanabe
Department of Chemical System Engineering, School of Engineering
The University of Tokyo
7-3-1 Hongo, Bunkyo-ku, Tokyo, Japan
E-mail: takanabe@chemsys.t.u-tokyo.ac.jp

Supporting information for this article is available on the WWW under https://doi.org/10.1002/cssc.202201088

© 2022 The Authors. ChemSusChem published by Wiley-VCH GmbH. This is an open access article under the terms of the Creative Commons Attribution Non-Commercial NoDerivs License, which permits use and distribution in any medium, provided the original work is properly cited, the use is non-commercial and no modifications or adaptations are made.

© 2022 The Authors. ChemSusChem published by Wiley-VCH GmbH

approaching the FE_{O_2} of 93%. In another example, Okada et al.[16] put an Mg-intercalated and Co-doped δ-type layered MnO_2 film on the α-$Co(OH)_2$ electrode. The upper Mg|Co-MnO_2 did not catalyze either the OER or the COR but worked as a permselective membrane that allowed for only H_2O molecules, rather than Cl^-, to access the underlying OER-active $Co(OH)_2$. The electrode achieved the FE_{O_2} of 79%. Notwithstanding these high FE values approaching the OER, this approach suffers from a decline in OER rates caused by the coating and reaches mere current densities of $< 100\ mA\,cm^{-2}$ at reasonable overpotentials that are not sufficient for industrial deployment. The second approach uses a vapor-fed cell that ensures a supply of pure evaporated H_2O from the seawater. Because the vapor consists only of H_2O, the COR does not proceed. Kumari et al.[17] proposed a PEM cell fed with vaporized seawater steam for the anode and dry N_2 for the cathode. However, achievable current densities were limited by diffusion of the reactant H_2O to the anode. Consequently, the cell was demonstrated to stably achieve only around $10\ mA\,cm^{-2}$ for 90 h, thus necessitating further development of a large-scale H_2 production system.

The third approach uses the thermodynamic potential gap between the OER and COR. The equations shown below [Eqs. (1)–(4)] dictate the OER and COR, including the hypochlorite formation reaction (HCFR), with corresponding thermodynamic standard potentials on the standard hydrogen electrode (SHE) or the reversible hydrogen electrode (RHE) scale:

$$2\ Cl^- \rightleftharpoons Cl_2 + 2e^-;\ E^0 = 1.36\ V\ vs.\ SHE \quad (1)$$

$$Cl^- + H_2O \rightleftharpoons HClO + H^+ + 2e^-;\ E^0 = 1.49\ V\ vs.\ SHE\ (pH\ 0) \quad (2)$$

$$Cl^- + H_2O \rightleftharpoons ClO^- + 2H^+ + 2e^-;\ E^0 = 1.72\ V\ vs.\ RHE \quad (3)$$

$$2H_2O \rightleftharpoons O_2 + 4H^+ + 4e^-;\ E^0 = 1.23\ V\ vs.\ RHE \quad (4)$$

While the potential gap between the OER and COR exists over a wide pH range, the gap value changes with pH levels. Below pH 7.5, at which the COR favors Cl_2 and HClO production [Eqs. (1) and (2)], the COR is thermodynamically allowed above 1.36 V vs. SHE while the OER occurs above 1.23 V vs. RHE, corresponding to the potential gap of 130 mV at pH 1 or 490 mV at pH 7.5. In contrast, at pH values above pH 7.5, the COR is dictated by Equation (3), and the potential gap remains at 490 mV irrespective of pH levels, thus leaving a range of conditions favorable for the OER expressed by Equation (4). Dionigi et al.[18] adopted this strategy at an alkaline pH level of 13. They used the $NiFeO_x$ electrode, a representative OER-active electrode,[19–21] and demonstrated a near-unity FE_{O_2} that remained stable for 2 h at $10\ mA\,cm^{-2}$ and approximately 1.71 V vs. RHE.

We consider that the "potential gap" approach would be more promising if less alkaline pH conditions could be adopted. Recently, near-neutral pH water electrolysis has appeared as an alternative to the alkaline processes. The near-neutral pH medium provides milder reaction conditions versus existing electrolysis systems that use extremely high pH levels. Therefore, this medium not only overcomes safety concerns but also reduces capital costs.[22] Nevertheless, near-neutral pH water electrolysis suffers from low cell efficiencies, and the recent decades have witnessed intensive research in this area. Nocera and co-workers investigated Co-,[23–25] Mn-,[26] or Ni-based[27,28] electrocatalysts at near-neutral pH levels and successfully detailed the OER mechanism. In another study, Görlin et al. examined the differences in the activity of the NiFe oxide between alkaline and mild pH levels, revealing the importance of the composition of Ni for the performance of the oxide.[29] Also, Bergmann et al. and Menezes et al. assessed cobalt oxide from the viewpoint of its structure[30] and morphology.[31] Furthermore, Strmcnik et al. studied the hydrogen oxidation reaction at near-neutral pH. They observed mass transfer-dependent plateaus, which indicated the current was strongly dependent on OH^- activity at pH values of 11 to 9.5.[32] Auinger et al.[33] investigated the surface pH levels during electrolysis both experimentally and theoretically at neutral pH levels and disclosed that adding the buffer substance suppresses the local pH shift. Our group quantitatively rationalized the influences of electrolyte identity and molality on the HER,[34] the OER,[35] and *iR* losses.[36,37] Moreover, our results revealed the participation of buffer substances in the reaction mechanism, thus highlighting the significance of the electrolyte engineering approach. Combining all efforts, near-neutral pH water electrolysis was demonstrated to reach $100\ mA\,cm^{-2}$ at 1.56 V and 373 K and remain stable for 24 h.[38] Notwithstanding these advancements, previous studies of seawater electrolysis have not included such engineering processes at near-neutral pH conditions.

This paper places emphasis on the thermodynamic approach for achieving hundreds of $mA\,cm^{-2}$ at near-neutral pH levels and reports on the discovery of a $CoFeO_xH_y$ electrode that serves as an active and stable electrocatalyst for the OER in the presence of Cl^-. Our initial assessment of the stability of the electrode substrate and electrolyte engineering clarified the conditions suitable for the OER at the $CoFeO_xH_y$ electrode. Furthermore, combined microkinetic and in-operando spectroscopic studies helped elucidate the active site and also indicated an enlarged surface area as the origin of improved activity when compared with CoO_xH_y and FeO_xH_y counterparts. For commercial applications, water electrolysis is conducted at high temperatures to obtain high current densities, especially for OER. The associated thermodynamic calculation reveals that the standard cell potential of the OER and the HCFR decreased to 1.18 and 1.71 V at 353 K, respectively. Therefore, the thermodynamic potential gap became 40 mV larger than that at room temperature, which had not been utilized in Cl^--containing buffered conditions. Using this temperature control strategy, the electrode achieved selective OER at $500\ mA\,cm^{-2}$, 1.67 V vs. RHE, and 353 K, outstanding the existing studies at near-neutral pH.

© 2022 The Authors. ChemSusChem published by Wiley-VCH GmbH

Results and Discussion

Fabrication and conditioning of $CoFeO_xH_y$ electrodes

During seawater electrolysis, local pH levels shift with appreciable current densities because the seawater does not have a high buffer capacity. This shift induces metal hydroxide precipitation as discussed in the Introduction and also switches reactants from proton (H^+) or hydroxide ions (OH^-) for the HER or OER, respectively, to stable H_2O thus lowering the cell efficiency.[39] Employing a buffer substance at pH levels closer to the pK_a maximizes the buffer capacity, wherein both HER and OER were reported to reach the maximum performances.[34,35] Among the available buffer substances, the organic ones are prone to oxidative degradation during aqueous electrolysis,[40] causing the inorganic ones, such as phosphate, borate, and carbonate, to be the applicable choice for practical use. The pK_a values of phosphate, borate, and carbonate are 7.2, 9.2, and 10.3, respectively, and the latter two allow for the widest potential gap between the OER and COR. Since borate has a pK_a value closer to near-neutral pH levels, it was selected as a model buffer substance in this study.

Choosing an appropriate electrode substrate is the key to stable electrolysis in the presence of Cl^-. The nickel-iron mixed oxide ($NiFeO_x$) electrode has been shown to exhibit high performance for the OER in alkaline pH aqueous medium[41] and is often deposited on the conductive material substrates.[42] Having high geometric surface area and affordability, metal substrates, such as nickel foam (NF), are commonly used as substrates.[43,44] When applied to Cl^--containing aqueous solutions, however, NF was reported to form metal chloride-hydroxide moieties via chloride aggression,[45–47] leading to its corrosion. The corrosion issue was also found to persist at pH 9.2. Employing $NiFeO_x$/NF as a model electrode, cyclic voltammograms (CVs) were recorded in 1.0 mol kg^{-1} potassium borate solution (K-borate) with or without 0.5 mol kg^{-1} KCl at pH 9.2. Our $NiFeO_x$/NF reached a current density of 10 mA cm^{-2} at 1.46 V vs. RHE in KOH electrolytes in agreement with the literature (Figure S1). In K-borate without Cl^- in Figure 1a, CVs over $NiFeO_x$/NF were stable with cycles reaching approximately 10 mA cm^{-2} at 1.63 V vs. RHE with *iR* correction and are consistent with the literature.[28] However, the presence of Cl^- caused drastic alterations to the current-potential relationship of $NiFeO_x$/NF. Figure 1b shows the CVs with 0.5 mol kg^{-1} added KCl in which successive cyclical changes were apparent. The observed anodic current densities were attributed to Cl^- absorption and formation of a metal-hydroxide complex,[46] indicating the corrosive behavior of $NiFeO_x$, NF, or both in the presence of Cl^-. Additional testing over pristine NF in Figure 1c disclosed successive changes that are also apparent without $NiFeO_x$. Furthermore, a green precipitate was observed on the electrode surface of both $NiFeO_x$/NF (Figure S2a) and NF (Figure S2b) after CV testing in the presence of Cl^-, which was absent after the testing over $NiFeO_x$/NF without Cl^- (Figure S2c). These observations indicate that the green precipitate was composed of Ni-hydroxide, a result that was supported by X-ray powder diffraction (XRD) measurement and shown in Figure S2d. Note that the precipitate did not form at the open circuit as in Figure S3, implying that the applied positive potentials were a prerequisite to its formation. Taken together, these observations concurrently pointed to the anodic corrosion of the NF that was induced by Cl^-. In contrast, titanium-based materials functioned as substrates without any noticeable corrosion (Figure S4), and the Ti felt was chosen hereafter as the electrode substrate.

Learning from the Pourbaix diagram and existing studies on the selective OER over Co-based electrodes[48,49] in addition to the enlarged OER rates of Co when modified with iron,[50] $CoFeO_xH_y$ on the Ti felt substrate was fabricated using an electrochemical deposition method. The deposition conditions of the Co/Fe nominal ratio and deposition time were optimized (see Figures S5 and S6); thus, the fabricated electrode was found to be stable during successive OER testing sessions (Figure S7; see below). In a previous study, Burke et al.[50] fabricated cobalt-iron hydroxide electrocatalysts using an electrodeposition method at −4.0 mA cm^{-2} that proceeded in nitrate-containing solutions, which we also use for making the $CoFeO_xH_y$. According to the authors, this deposition proceeds via the cathodic reduction of NO_3^- at the electrode surface, which leads to an increase in the pH to drive metal hydroxide precipitation at the electrode surface. In our study, electrodeposition proceeded under constant negative current density

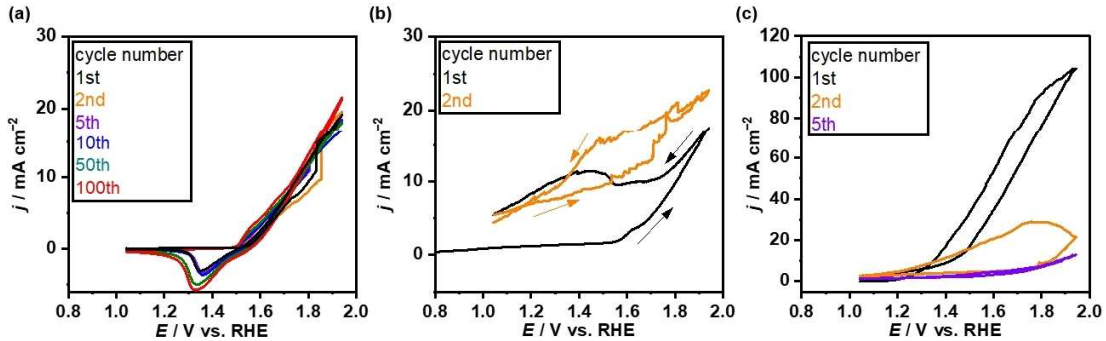

Figure 1. Stability testing of NF by CV. CVs over $NiFeO_x$/NF in (a) 1.0 mol kg^{-1} K-borate at pH 9.2, or (b) 1.0 mol kg^{-1} K-borate + 0.5 mol kg^{-1} KCl at pH 9.2. (c) CVs over NF in 1.0 mol kg^{-1} K-borate + 0.5 mol kg^{-1} KCl at pH 9.2. All measurements were performed at 298 K, O_2 bubbling, at a scan rate of 1 mV s^{-1} and recorded immediately after immersing the electrode in solutions to eliminate the possible dissolution of electrocatalyst.

© 2022 The Authors. ChemSusChem published by Wiley-VCH GmbH

at −10 mA cm^{-2}, the rate of which was likely to be high enough to cause a similar reaction, and thus cobalt-iron hydroxide was expected to deposit on the substrate. This consideration is supported by several characterizations. The as-synthesized $CoFeO_xH_y$/Ti matched that of the pristine Ti substrate (Figure S8), except for the one at 18.2° attributed to (001) of $Co(OH)_2$,[51] indicating the mostly amorphous nature of synthesized $CoFeO_xH_y$. Closer inspection by transmission electron microscopy (TEM) indicates the aggregation of nano-sized domains over $CoFeO_xH_y$ as shown in Figure 2b,d,f. The scanning electron microscope–energy dispersive X-ray (SEM–EDX) images of as-made catalysts show the flake-like morphology with a homogeneous distribution of cobalt and iron (Figure 2a), which is consistent with the typically observed morphology for metal hydroxide and reported cobalt-iron hydroxide electrocatalysts.[50,52,53] In addition, X-ray photoelectron spectroscopy (XPS) analysis in Figure 2g,h revealed the shift of the peak top position of Co 2p and Fe 2p[54] when Co and Fe are mixed. This result indicates the intercalation of the Fe into the $Co(OH)_2$ framework. This observation agrees well with the previous report. On the Raman spectra shown in Figure 2i, the $CoFeO_xH_y$/Ti shows peaks at 180, 455, 500, 590, and 660 cm^{-1}. Because these peaks were also observed over a control electrode composed of CoO_xH_y but distinct from those observed over another control composed of FeO_xH_y, the electrode surface was similar to that of CoO_xH_y. The peaks at 180, 500, and 660 cm^{-1} were thus attributed to F_{2g}, A_g, and A_{1g} modes of CoO, respectively, while the peaks at 455 and 590 cm^{-1} were attributable to O–Co–O vibration.[55,56] These observations suggest that the $CoFeO_xH_y$ electrode was composed of crystalline $Co(OH)_2$ together with amorphous Fe^{2+}, Fe^{3+}, and Co^{3+} (hydr)oxides phases. According to the inductively coupled plasma (ICP) analysis, the electrode was composed of 1.4 mg of Co and 0.6 mg of Fe.

Employing $CoFeO_xH_y$/Ti as a model electrode, electrolyte engineering was subsequently conducted to maximize the electrocatalytic performance. Figure 3a shows linear-sweep voltammograms (LSVs) over the $CoFeO_xH_y$/Ti at a scan rate of 1 mV s^{-1} in varying molalities of K-borate ranging from 0.1 to 1.9 mol kg^{-1} (saturated). Irrespective of molalities, the anodic current densities were apparent above approximately 1.55 V vs. RHE, which was attributed to the OER. Higher current densities were reached at higher molalities, most likely due to the improved buffer capacity.[33] Notably, the current-potential relationship remained unchanged above 1.0 mol kg^{-1}; thus, the threshold concentration of 1.0 mol kg^{-1} was chosen for further study. Interestingly, the identity of the cation did not significantly influence the behavior of $CoFeO_xH_y$/Ti. Figure 3b shows LSV values in electrolytes containing 1.0 mol kg^{-1} Li-, Na-, K-, or Cs-borate at a scan rate of −1 mV s^{-1}. This molality exceeded

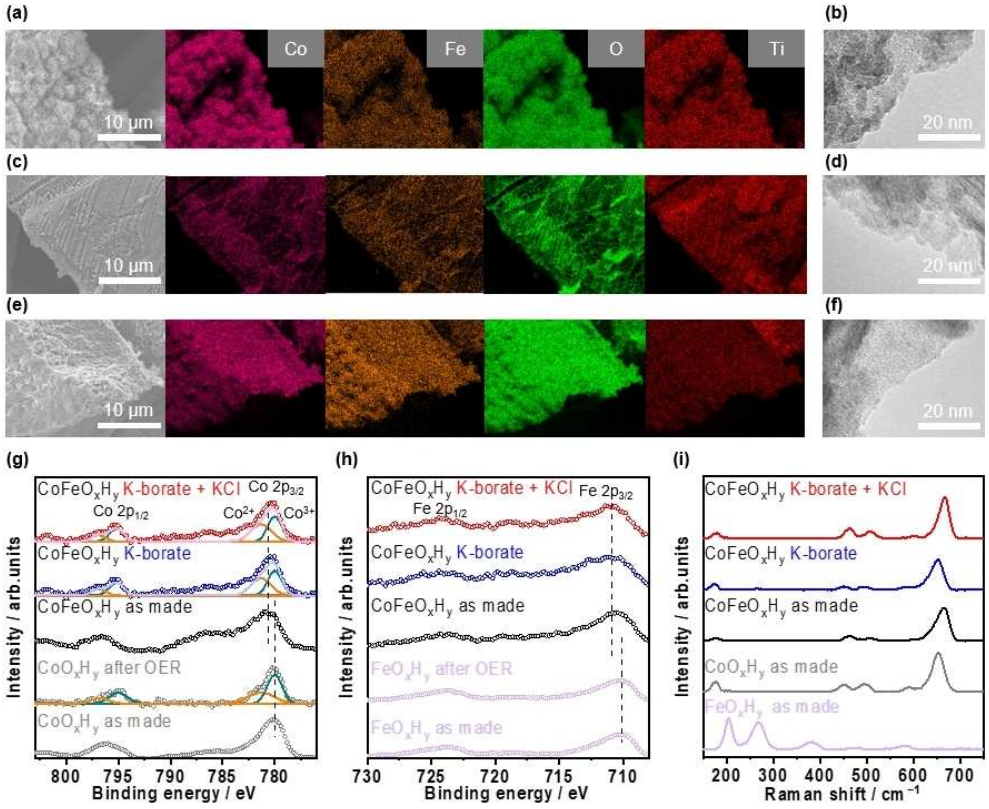

Figure 2. Ex-situ characterization of $CoFeO_xH_y$/Ti before or after OER testing. SEM images with corresponding EDX mappings of (a) as-made, (c) after OER testing in 1.0 mol kg^{-1} K-borate, and (e) after OER testing in 1.0 mol kg^{-1} K-borate + 0.5 mol kg^{-1} KCl of $CoFeO_xH_y$. TEM images of (b) as-made, (d) after OER testing in 1.0 mol kg^{-1} K-borate, and (f) after OER testing in 1.0 mol kg^{-1} K-borate + 0.5 mol kg^{-1} KCl of $CoFeO_xH_y$. XPS in (g) Co 2p, (h) Fe 2p regions. OER testing was conducted with chronopotentiometry (CP) at 50 mA cm^{-2} for 1 h at 298 K. (i) Raman spectrum.

© 2022 The Authors. ChemSusChem published by Wiley-VCH GmbH

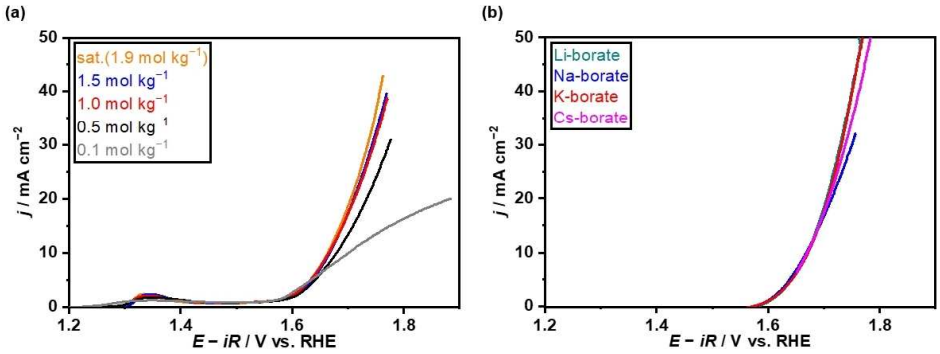

Figure 3. Electrolyte engineering for the OER in K-borate solutions over $CoFeO_xH_y$/Ti. LSV profiles in (a) 0.1, 0.5, 1.0, 1.5, or 1.9 mol kg^{-1} (saturated) K-borate at pH 9.2, and (b) in 1.0 mol kg^{-1} Li-, Na-, K-, or Cs-borate at pH 9.2. All measurements were performed at 298 K, O_2 bubbling.

the solubility product of Na-borate, which most likely accounted for the observed lessened current densities in Na-borate than others. In other electrolytes of Li-, K-, or Cs-borate, the current-potential relationships mostly overlapped. The reason for the insensitivity is not immediately clear, but it is postulated that these cationic species might not affect the superoxo OER intermediate.[57] Knowing the impact of electrolytes on the anodic behavior of $CoFeO_xH_y$/Ti, K-borate at 1.0 mol kg^{-1} was chosen for further kinetic studies.

By employing $CoFeO_xH_y$ in a 1.0 mol kg^{-1} K-borate electrolyte solution, the influence of different potentials on the OER and COR were investigated. FE_{O_2} was determined by on-line gas chromatography (GC) as shown in Figure S9. In detail, the experiments were conducted at each current density (20 and 50 mA cm^{-2}) corresponding to the potentials (1.72 and 1.82 V vs. RHE) for 1 h at room temperature. In addition, FE toward hypochlorite (FE_{HC}) was calculated based on the concentration of ClO^- remained after gas evaluation testing in the solution as determined by *N,N*-diethyl-*p*-phenylenediamine (DPD) method (see Figure S10). Below the standard potential of ClO^- formation at 1.72 V vs. RHE denoted by the pink line in Figure 4a, current-potential relationships were found to be insensitive to the Cl^- and exhibited a Tafel slope value of approximately 100 mV dec^{-1}. At 1.72 V vs. RHE in the presence of Cl^-, the FE_{O_2} reached 98 ± 1 %, whereas the FE_{HC} was merely 1 ± 1 %. Above this threshold potential, the COR started to influence the anodic behavior. Quantitatively, our chronopotentiometry (CP) testing at 50 mA cm^{-2} corresponding to approximately 1.82 V vs. RHE with Cl^- as shown in Figure 4a, FE_{O_2} decreased to 93 ± 2 % while FE_{HC} increased to 7 ± 2 %. Interestingly, the potential of 1.82 V was found to be larger than 1.78 V observed without Cl^-, likely suggestive of blockage of the OER active site by Cl^- or related species.[58] Long-term CP testing as shown in Figure 4b disclosed stable behavior of electrodes below 1.72 V vs. RHE for at least 42 h, but potential gradually increased above this threshold. Black precipitates were observed at the bottom of the cell after this CP testing at 50 mA cm^{-2}, which was suggested to be a metal chloride-hydroxide complex by XRD (Figure S8c). This catalytic testing revealed that the $CoFeO_xH_y$/Ti electrode directs the reaction almost exclusively toward the OER in the presence of Cl^-.

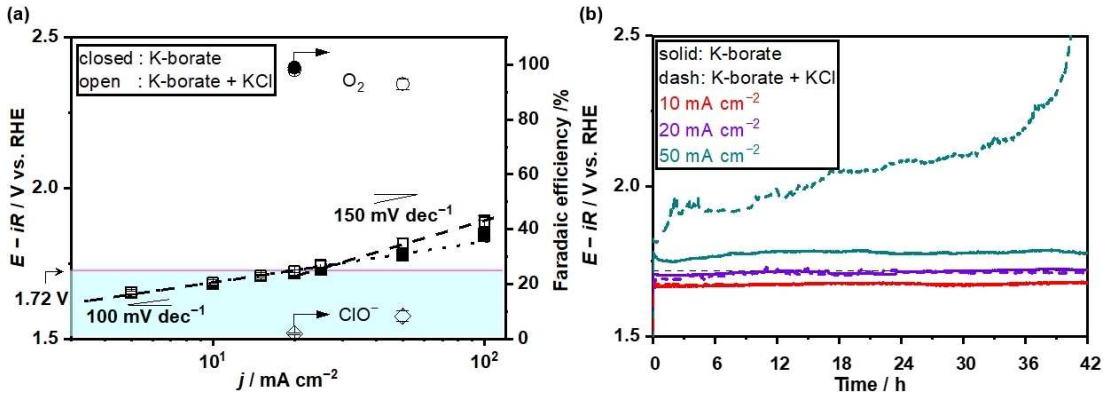

Figure 4. Evaluation of OER performance over $CoFeO_xH_y$/Ti. (a) Tafel plots determined by CP for 15 min at each current, and corresponding FE of O_2 and hypochlorite determined by on-line GC and DPD method. (b) Long-term CP testing at a designated current density of 10, 20, or 50 mA cm^{-2} in O_2-saturated 1.0 mol kg^{-1} K-borate with or without 0.5 mol kg^{-1} KCl. All measurements were performed at 298 K.

© 2022 The Authors. ChemSusChem published by Wiley-VCH GmbH

Kinetic and operando spectroscopic analysis

The microkinetic analysis helped detail the roles of Co and Fe present in $CoFeO_xH_y$/Ti electrodes. Our Tafel analysis in Figure 5 discloses similar Tafel slope values of 120 ± 2, 137 ± 4, and 110 ± 5 mV dec^{-1} for CoO_xH_y, FeO_xH_y, and $CoFeO_xH_y$, respectively, at 298 K. Note that the Tafel analysis for $CoFeO_xH_y$ in Figure 5a was conducted below the HCFR potential to eliminate the influence of the partial current density originating from the COR. The temperature sensitivities of electrodes were assessed in Figure 5d in which the exchange current density (j_0), was plotted as a function of the reciprocal of the temperature. The figure revealed similar slope values among electrodes. Generally speaking, j_0 in a simple form can be expressed using the Equation (5) shown below:

$$j_0 = nFCk^0 \tag{5}$$

in which n is the number of the electron, F is Faraday's constant, C is the concentration of reactant, and k_0 is the standard rate constant. The k^0 is described by Equation (6):

$$k^0 = A' \exp\left(-\frac{E_{a,app}}{RT}\right) \tag{6}$$

in which A' is the pre-exponential factor, and $E_{a,app}$ is the apparent activation energy. Therefore, the slope of j_0–T^{-1} plot corresponds to $E_{a,app}$ as in the following Equation (7) derived from Equations (5) and (6):

$$\frac{\partial \ln(j_0)}{\partial(1/T)} = -\frac{E_{a,app}}{RT} \tag{7}$$

According to this analysis, the $E_{a,\ app}$ over CoO_xH_y, FeO_xH_y, and $CoFeO_xH_y$ were determined to be 45, 38, and 41 kJ mol^{-1}, respectively, in K-borate electrolyte without Cl^- and that of $CoFeO_xH_y$ in the presence of Cl^- was calculated to be 43 kJ mol^{-1}. The similar values from both Tafel slopes and apparent activation energies among electrodes indicate similar active sites and reaction mechanisms over these electrodes. It was envisaged that Co and Fe are similar under the investigated conditions, and mixed oxides of $CoFeO_xH_y$ did not alter such sites. On the contrary, the addition of Fe was found to cause a drastic enlargement of the double-layer capacitance (C_{dl}) of electrodes. Quantitatively, Figure 5e illustrates that C_{dl} increased by 3-fold (see Figure S11 for original CVs). These findings suggest that the OER performance of $CoFeO_xH_y$ did not originate from the improved nature of active sites but rather from the increased number of active sites. The amount of loaded catalyst is an important parameter for OER performance. A detailed discussion is made based on the data shown in Figure S12 to support our argument for C_{dl}. This rationale contrasts the reported Fe-modified Co electrode in KOH solutions.[50] For instance, Smith et al.[59–61] proposed that di-μ-oxo bridged Co–Fe sites act as active sites above a transition voltage, and below that value, di-μ-oxo bridged Co–Co works as an active site. Incorporating Fe into the CoO_x fosters the

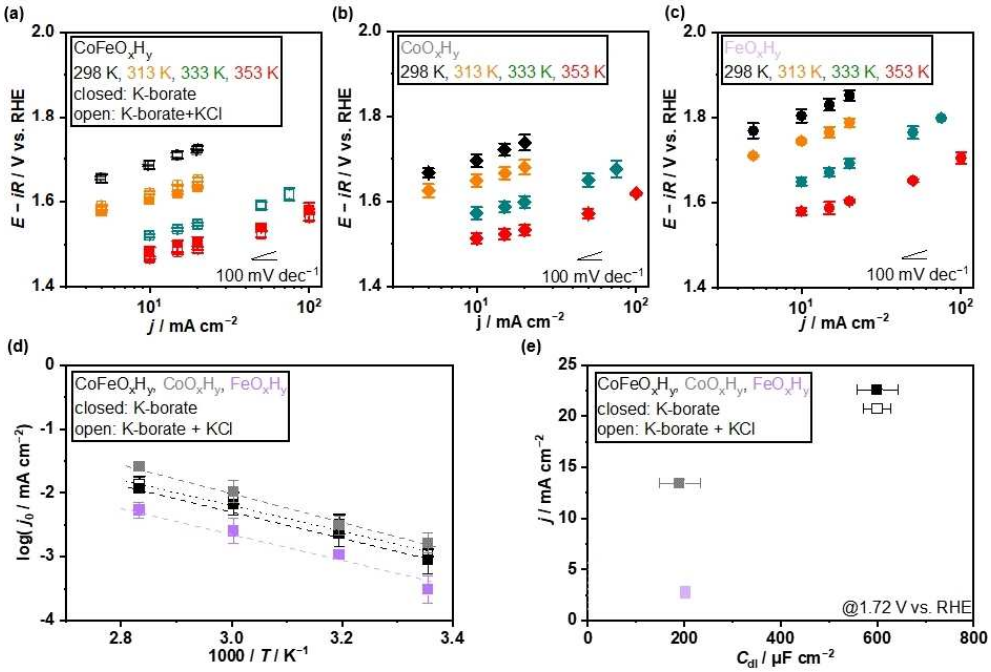

Figure 5. Kinetic analysis over distinct electrocatalyst. Tafel slopes for (a) $CoFeO_xH_y$, (b) CoO_xH_y, (c) FeO_xH_y at steady state obtained from CP profiles at various temperature of 298, 313, 333, or 353 K in (closed) 1.0 mol kg^{-1} K-borate, (open) 1.0 mol kg^{-1} K-borate + 0.5 mol kg^{-1} KCl with O_2 bubbling. (d) Arrhenius plot for three electrocatalysts obtained from Tafel plot (a–c). (e) Current density and C_{dl} relationship. The current density was obtained from LSV at a scan rate −1 mV s^{-1}. C_{dl} values were calculated from the result of currents at suitable voltage vs. RHE as a function of scan rate.

© 2022 The Authors. ChemSusChem published by Wiley-VCH GmbH

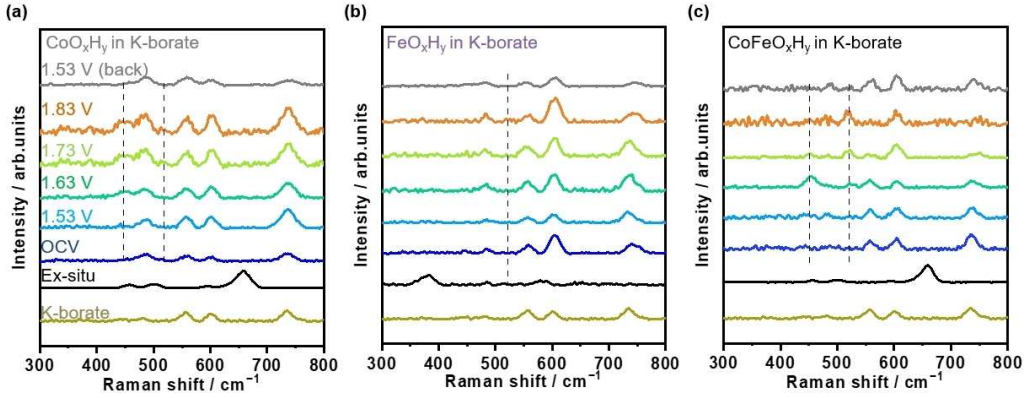

Figure 6. In-*operando* Raman spectra of various electrodes. Raman spectrum of (a) CoO_xH_y, (b) FeO_xH_y, (c) $CoFeO_xH_y$ recorded in 1.0 mol kg^{-1} K-borate at 298 K. The vertical dashed lines are added as a visual guide.

formation of active species, likely $Co^{III}Fe^{III}OOH$, whose OER activity is better than that of CoO_x.[62]

Post-reaction samples were initially characterized *ex-situ*. SEM–EDX in Figure 2 visualized the homogeneous distribution of Fe and Co species that were preserved after testing. The Raman spectra in Figure 2g did not capture changes in vibrations, and the XPS spectra in Figures 3h,i revealed similar chemical states of the electrode surface before and after OER testing, consisting of 2+/3+ for both Co and Fe.

Operando Raman spectroscopy was carried out to obtain insight into the active sites of $CoFeO_xH_y$/Ti. Figure 6 summarizes the spectra recorded at open-circuit potential followed by applied potentials from 1.53 to 1.83 V with an increment of 0.1 V, and back to 1.53 V vs. RHE. The figure also shows reference spectra of K-borate solution with peaks at 558, 601, and 736 cm^{-1}, attributed to $[B_5O_6(OH)_4]^-$, $[B_3O_3(OH)_4]^-$, and $[B(OH)_4]^-$, respectively.[63] The control CoO_x sample in Figure 6a exhibited a peak at 490 cm^{-1} that was assigned to CoO,[55,56] in addition to peaks attributed to the electrolyte at the open circuit. At 1.63 V, a peak appeared at 450 cm^{-1}, consistent with the literature on cobalt oxide at alkaline pH, and thus was assigned to CoO_2.[64–66] At higher potentials of 1.73 V, an additional peak emerged at 520 cm^{-1} attributed to CoOOH.[20] Notably, while the potential-dependent metal oxide species were observed, no evidence could be observed for active oxygen species such as superoxide at 800–1200 cm^{-1}, presumably due to its short-lived nature at near-neutral pH levels.[67] Regarding the control FeO_xH_y electrode in Figure 6b, a peak was observed at around 490 cm^{-1} at open-circuit potentials, attributed to Fe_2O_3.[68,69] When the electrode potential was increased to 1.83 V, a new peak appeared at approximately 520 cm^{-1}, which might have been FeOOH.[20] The spectra of $CoFeO_xH_y$/Ti contained a mixture of these spectra. In Figure 6c, $CoFeO_xH_y$ showed a peak at 450 cm^{-1} at open-circuit, attributable to CoO_2 as described in Figure 6a. At applied potentials of 1.63 V, an additional peak appeared at 520 cm^{-1}, indicative of the formation of CoOOH, FeOOH, or both. Of note, these spectral features were not affected by the presence of Cl^- (see Figure S13 for spectra with added Cl^-). Because no additional peaks or apparent peak shifts were observed, this spectral evidence supports our claim that the $CoFeO_xH_y$ benefited from the increased number of active Co-, Fe-, or both sites.

Last, targeting practical applications, the OER performance was assessed at an elevated temperature of 353 K over the herein developed $CoFeO_xH_y$/Ti. Our calculations on thermodynamics revealed that standard potentials of OER decreased to 1.18 V vs. RHE at 353 K, while that of HCFR was 1.71 V vs. RHE at 353 K, leaving a potential gap of 530 mV (see Figure S14 for calculated values). The impact of increasing temperatures on selective OER in the presence of Cl^- has not been described well in the literature. The enlarged potential gap at an elevated temperature between OER and HCER would propose the "potential gap" approach to be a good option for selective OER. In this context, CP testing data at 500 mA cm^{-2} and 353 K are plotted in Figure 7, disclosing that a mere voltage of 1.67 V vs. RHE was sufficient to drive the OER at this rate, which was consistently measured as FE_{O_2} of 99±2% because the potential was within the threshold. Also, the stability of the electrode is another important index for aiming the commercial applica-

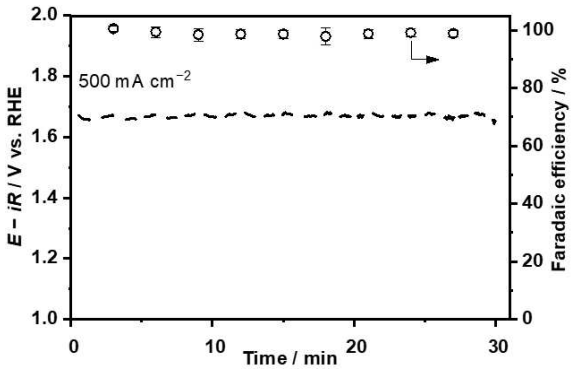

Figure 7. Evaluation of FE_{O_2} over $CoFeO_xH_y$/Ti using CP at elevated temperature. *iR*-corrected potential at 500 mA cm^{-2} and corresponding FE toward the OER plotted as measurement time. The measurement was conducted in a two-compartment cell separated by a glass frit, filled with 1.0 mol kg^{-1} K-borate + 0.5 mol kg^{-1} KCl at pH 9.2 and 353 K.

© 2022 The Authors. ChemSusChem published by Wiley-VCH GmbH

tions. We investigated the stability by on-off cycle and long-term (24 h) testing at 500 mA cm^{-2} and 353 K. The electrode retained its integrity during the testing (see Figure S15a,b). This result is outstanding among reported values at near-neutral pH levels in the presence of Cl^-, as summarized in Figure S16.

Conclusions

The present study reports on the $CoFeO_xH_y$ electrode that can stably electro-catalyze the oxygen evolution reaction (OER) in an aqueous K-borate solution at pH 9.2 in the presence of Cl^-. The Ni substrate was corroded by Cl^- at applied potentials, whereas the Ti substrate was highly tolerant to it. An electrolyte engineering study revealed a molality of 1.0 mol kg^{-1} to be sufficient to retain the buffer capacity irrespective of cation identity except for the Na cation counterpart having a low solubility product. The fabricated $CoFeO_xH_y$/Ti electrode was found to possess a $Co(OH)_2$ crystalline structure, and mixed $Co^{2+/3+}$ and $Fe^{2+/3+}$ (hydr)oxide phases were homogeneously distributed over the surface. Our kinetic study revealed that Tafel slopes and apparent activation energies of $CoFeO_xH_y$ resembled the control CoO_xH_y and FeO_xH_y electrodes. Likewise, *operando* Raman spectroscopy disclosed no additional peaks or apparent peak shifts over $CoFeO_xH_y$ compared with the controls. These findings suggest that the OER performance of $CoFeO_xH_y$ did not originate from the improved nature of the active site but rather from the increased number of active sites. Our thermodynamic calculation shows that the potential gap between the OER and the hypochlorite formation reaction at 353 K becomes 40 mV larger than that at room temperature. Using this temperature control, the electrode developed in this study reached 500 mA cm^{-2} at 1.67 V vs. reversible hydrogen electrode and 353 K with an almost unity faradaic efficiency towards O_2, outperforming the OER performance reported in the literature at near-neutral pH levels.

Experimental Section

Materials and chemicals

NF (thickness 1.6 mm, pore size 0.5 mm, 48–52 cells inch^{-1}, 7500 m^2 m^{-3}) and Pt wire were purchased from Nilaco Corporation. Ti felt (thickness 0.1–30 mm, pore size 15–80 μm, porosity 50–80%) was purchased by Nkkotechno corporation. KCl-saturated Ag/AgCl and Hg/HgO reference electrodes were purchased by BAS Inc. DPD reagent was purchased by Kazusa Corporation. All chemicals were purchased with purities from FUJIFILM Wako unless otherwise specified: LiOH (>98, Sigma-Aldrich), NaOH (>98%, Sigma-Aldrich), KOH (>85%, Sigma-Aldrich), CsOH (>99%, Sigma-Aldrich), $Ni(NO_3)_2\cdot 6H_2O$ (99.9%), $Fe(NO_3)_3\cdot 9H_2O$ (99.9%), $Co(NO_3)_2\cdot 6H_2O$ (99.5%), $CO(NH_2)_2$ (>99.0%, Sigma-Aldrich), H_3BO_3 (99.5%, Sigma-Aldrich), HCl(35–37%), $NaClO_4$ (effective chlorine >5%). Iron standard solution (Fe 1000), Co standard solution (Fe 1000). Ar (99.9999%) and O_2 (99.99995%) gases were used. Ultrapure water was used for the preparation of all aqueous solutions.

Electrolyte preparation

Electrolyte solutions were prepared according to several steps. First, the buffering compound was dissolved as the number of required kg in distilled water to yield the desired concentration (mol kg^{-1}) after which the pH was adjusted by adding the necessary M(OH) (M=Li, Na, K, Cs) powder until the pH reached 9.2. For the solution containing KCl, the salt was added to the solution before adjusting the pH.

Electrochemical measurement

Three-electrode systems were used for electrochemical measurements. In all half-cell measurements, Pt wire was used as a counter electrode. A KCl-saturated Ag/AgCl electrode was used as a reference electrode. Note that a Hg/HgO reference electrode was used in alkaline pH conditions. Before and during all measurements, the specified gas (O_2 for the OER and Ar for double-layer and FE measurements) was supplied to the cell. Electrochemical measurements were performed at various temperatures while keeping the reference electrode at 298 K using a 16-channel, research-grade potentiostat system (VMP3; BioLogic Science Instruments) or a 1-channel potentiostat system (SP-150; BioLogic Science Instruments). The cell used for the high temperature (>298 K) test was equipped with a water jacket (water-jacketed glass cell; BAS Inc.). The liquid was passed around the jacket and heated to the electrolyte, the temperature of which was controlled using an external temperature control system (NCB-1210 A, EYELA). All current–potential relationships described in this paper, except those in Figure 1, were *iR*-corrected using the measured impedance values (≥100 kHz, amplitude 10 mV).

Electrode preparation

$NiFeO_x$/NF: $NiFeO_x$/NF was synthesized by hydrothermal treatment following the method described in the literature.[70] First, 1.96 mmol $Ni(NO_3)_2$, 1.88 mmol $Fe(NO_3)_3$, and 9.50 mmol $CO(NH_2)_2$ were mixed in 152 mL of Milli-Q water (18.2 MΩ cm) under vigorous stirring at room temperature for 10 min. The solution was transferred to a 190 mL Teflon-lined stainless-steel autoclave where the NF substrates were immersed. The sealed autoclave was placed in an oven and heat-treated at 393 K for 12 h.

CoO_xH_y, FeO_xH_y, and $CoFeO_xH_y$/Ti: Before conducting the electrochemical deposition, Ti felt was washed with HCl until bubbles were generated, then washed with EtOH. Electrodeposition was carried out in a three-electrode system with working electrode, counter electrode (Pt wire), and reference electrode (Ag/AgCl, sat. KCl). Constant current density −10 mA cm^{-2} was applied to the masked working electrode (Ti felt 1×1 cm^2) in the various concentration of $Fe(NO_3)_3\cdot 9H_2O$ and $Co(NO_3)_2\cdot 6H_2O$. The prepared solution was 15 mL. After deposition, the electrode was washed with water.

Faradaic efficiency calculation

For gas evaluation, especially O_2, we employed a two-chamber frit cell. Two-room was separated by a glass flit which can pass the solution, but evolved gas, which was connected to a GC (GC-8 A; Shimadzu Co. Ltd.) equipped with a thermal conductivity detector (TCD) and a Molecular Sieve 5 A column using Ar gas as a carrier gas. The FE was calculated based on the measured O_2 generation rate in mol. For evaluating the FE of hypochlorite, which evolved after the gas evaluation test in the cell, we used DPD powder. For the remaining electrolyte, 0.1 mL was taken and diluted with water until the total amount reached 10 mL, after which DPD powder was

© 2022 The Authors. ChemSusChem published by Wiley-VCH GmbH

added. DPD absorbed light and solution became the pink. The intensity of the absorbance recorded by UV/Vis spectroscopy corresponded to the number of hypochlorite ions. The absorbance related to hypochlorite ions is known to increase over time; thus, we obtained the spectrum for 3 min after adding the powder.

Acknowledgments

Part of this work was supported by JSPS KAKENHI Grant Number 19KK0126 and the Mohammed bin Salman Center for Future Science and Technology for Saudi-Japan Vision 2030 at The University of Tokyo (MbSC2030)

Conflict of Interest

The authors declare no conflict of interest.

Data Availability Statement

The data that support the findings of this study are available from the corresponding author upon reasonable request.

Keywords: electrocatalysis · electrochemistry · electrolytes · seawater · water splitting

[1] M. F. Lagadec, A. Grimaud, *Nat. Mater.* **2020**, *19*, 1140–1150.
[2] Y. Nakajima, N. Fujimoto, S. Hasegawa, T. Usui, *ECS Trans.* **2017**, *80*, 835.
[3] I. C. Karagiannis, P. G. Soldatos, *Desalination* **2008**, *223*, 448–456.
[4] C. J. Vorosmarty, P. Green, J. Salisbury, R. B. Lammers, *Science* **2000**, *289*, 284–288.
[5] C. J. Vörösmarty, P. B. McIntyre, M. O. Gessner, D. Dudgeon, A. Prusevich, P. Green, S. Glidden, S. E. Bunn, C. A. Sullivan, C. R. Liermann, *Nature* **2010**, *467*, 555–561.
[6] W. Tong, M. Forster, F. Dionigi, S. Dresp, R. Sadeghi Erami, P. Strasser, A. J. Cowan, P. Farràs, *Nat. Energy* **2020**, *5*, 367–377.
[7] L.-Q. Jiang, B. R. Carter, R. A. Feely, S. K. Lauvset, A. Olsen, *Sci. Rep.* **2019**, *9*, 18624.
[8] E. M. Kapp, *Biol. Bull.* **1928**, *55*, 453–458.
[9] S. Dresp, F. Dionigi, S. Loos, J. Ferreira de Araujo, C. Spöri, M. Gliech, H. Dau, P. Strasser, *Adv. Energy Mater.* **2018**, *8*, 1800338.
[10] A. Kraft, M. Stadelmann, M. Blaschke, D. Kreysig, B. Sandt, F. Schroder, J. Rennau, *J. Appl. Electrochem.* **1999**, *29*, 861–868.
[11] J. G. Vos, M. T. M. Koper, *J. Electroanal. Chem.* **2018**, *819*, 260–268.
[12] K. Izumiya, E. Akiyama, H. Habazaki, N. Kumagai, A. Kawashima, K. Hashimoto, *Electrochim. Acta* **1998**, *43*, 3303–3312.
[13] K. Fujimura, K. Izumiya, A. Kawashima, E. Akiyama, H. Habazaki, N. Kumagai, K. Hashimoto, *J. Appl. Electrochem.* **1999**, *29*, 765–771.
[14] N. A. Abdel Ghany, N. Kumagai, S. Meguro, K. Asami, K. Hashimoto, *Electrochim. Acta* **2002**, *48*, 21–28.
[15] J. G. Vos, T. A. Wezendonk, A. W. Jeremiasse, M. T. Koper, *J. Am. Chem. Soc.* **2018**, *140*, 10270–10281.
[16] T. Okada, H. Abe, A. Murakami, T. Shimizu, K. Fujii, T. Wakabayashi, M. Nakayama, *Langmuir* **2020**, *36*, 5227–5235.
[17] S. Kumari, R. T. White, B. Kumar, J. M. Spurgeon, *Energy Environ. Sci.* **2016**, *9*, 1725–1733.
[18] F. Dionigi, T. Reier, Z. Pawolek, M. Gliech, P. Strasser, *ChemSusChem* **2016**, *9*, 962–972.
[19] D. Friebel, M. W. Louie, M. Bajdich, K. E. Sanwald, Y. Cai, A. M. Wise, M.-J. Cheng, D. Sokaras, T.-C. Weng, R. Alonso-Mori, *J. Am. Chem. Soc.* **2015**, *137*, 1305–1313.
[20] M. W. Louie, A. T. Bell, *J. Am. Chem. Soc.* **2013**, *135*, 12329–12337.
[21] J. Luo, J.-H. Im, M. T. Mayer, M. Schreier, M. K. Nazeeruddin, N.-G. Park, S. D. Tilley, H. J. Fan, M. Grätzel, *Science* **2014**, *345*, 1593–1596.
[22] D. G. Nocera, *ChemSusChem* **2009**, *2*, 387–390.
[23] Y. Surendranath, M. Dincă, D. G. Nocera, *J. Am. Chem. Soc.* **2009**, *131*, 2615–2620.
[24] T. P. Keane, D. G. Nocera, *ACS Omega* **2019**, *4*, 12860–12864.
[25] A. J. Esswein, Y. Surendranath, S. Y. Reece, D. G. Nocera, *Energy Environ. Sci.* **2011**, *4*, 499–504.
[26] M. Huynh, C. Shi, S. J. Billinge, D. G. Nocera, *J. Am. Chem. Soc.* **2015**, *137*, 14887–14904.
[27] M. Dincă, Y. Surendranath, D. G. Nocera, *Proc. Natl. Acad. Sci. USA* **2010**, *107*, 10337–10341.
[28] D. K. Bediako, Y. Surendranath, D. G. Nocera, *J. Am. Chem. Soc.* **2013**, *135*, 3662–3674.
[29] M. Görlin, M. Gliech, J. F. de Araújo, S. Dresp, A. Bergmann, P. Strasser, *Catal. Today* **2016**, *262*, 65–73.
[30] A. Bergmann, T. E. Jones, E. M. Moreno, D. Teschner, P. Chernev, M. Gliech, T. Reier, H. Dau, P. Strasser, *Nat. Catal.* **2018**, *1*, 711–719.
[31] P. W. Menezes, A. Indra, D. González-Flores, N. R. Sahraie, I. Zaharieva, M. Schwarze, P. Strasser, H. Dau, M. Driess, *ACS Catal.* **2015**, *5*, 2017–2027.
[32] D. Strmcnik, M. Uchimura, C. Wang, R. Subbaraman, N. Danilovic, D. van der Vliet, A. P. Paulikas, V. R. Stamenkovic, N. M. Markovic, *Nat. Chem.* **2013**, *5*, 300–306.
[33] M. Auinger, I. Katsounaros, J. C. Meier, S. O. Klemm, P. U. Biedermann, A. A. Topalov, M. Rohwerder, K. J. Mayrhofer, *Phys. Chem. Chem. Phys.* **2011**, *13*, 16384–16394.
[34] K. Obata, L. Stegenburga, K. Takanabe, *J. Phys. Chem. C* **2019**, *123*, 21554–21563.
[35] T. Nishimoto, T. Shinagawa, T. Naito, K. Takanabe, *ChemSusChem* **2021**, *14*, 1554–1564.
[36] T. Shinagawa, K. Takanabe, *J. Phys. Chem. C* **2016**, *120*, 1785–1794.
[37] T. Naito, T. Shinagawa, T. Nishimoto, K. Takanabe, *ChemSusChem* **2020**, *13*, 5921–5933.
[38] T. Naito, T. Shinagawa, T. Nishimoto, K. Takanabe, *ChemSusChem* **2022**, *15*, e202102294.
[39] D. Strmcnik, M. Uchimura, C. Wang, R. Subbaraman, N. Danilovic, D. Van Der Vliet, A. P. Paulikas, V. R. Stamenkovic, N. M. Markovic, *Nat. Chem.* **2013**, *5*, 300–306.
[40] H. Nonaka, Y. Matsumura, *J. Electroanal. Chem.* **2002**, *520*, 101–110.
[41] F. Dionigi, P. Strasser, *Adv. Energy Mater.* **2016**, *6*, 1600621.
[42] H. Zhou, F. Yu, Q. Zhu, J. Sun, F. Qin, L. Yu, J. Bao, Y. Yu, S. Chen, Z. Ren, *Energy Environ. Sci.* **2018**, *11*, 2858–2864.
[43] X. Lu, C. Zhao, *Nat. Commun.* **2015**, *6*, 6616.
[44] X. Liu, X. Wang, X. Yuan, W. Dong, F. Huang, *J. Mater. Chem. A* **2016**, *4*, 167–172.
[45] J. Juodkazytė, B. Šebeka, I. Savickaja, M. Petrulevičienė, S. Butkutė, V. Jasulaitienė, A. Selskis, R. Ramanauskas, *Int. J. Hydrogen Energy* **2019**, *44*, 5929–5939.
[46] T. Ma, W. Xu, B. Li, X. Chen, J. Zhao, S. Wan, K. Jiang, S. Zhang, Z. Wang, Z. Tian, Z. Lu, L. Chen, *Angew. Chem. Int. Ed.* **2021**, *60*, 22740–22744; *Angew. Chem.* **2019**, *131*, 13133–13137.
[47] Y. Kuang, M. J. Kenney, Y. Meng, W.-H. Hung, Y. Liu, J. E. Huang, R. Prasanna, P. Li, Y. Li, L. Wang, M.-C. Lin, M. D. McGehee, X. Sun, H. Dai, *Proc. Natl. Acad. Sci. USA* **2019**, *116*, 6624–6629.
[48] A. Badreldin, A. Nabeeh, E. Youssef, N. Mubarak, H. ElSayed, R. Mohsen, F. Ahmed, Y. Wubulikasimu, K. Elsaid, A. Abdel-Wahab, *ACS Appl. Mater. Interfaces* **2021**, *4*, 6942–6956.
[49] A. J. Esswein, Y. Surendranath, S. Y. Reece, D. G. Nocera, *Energy Environ. Sci.* **2011**, *4*, 499–504.
[50] M. S. Burke, M. G. Kast, L. Trotochaud, A. M. Smith, S. W. Boettcher, *J. Am. Chem. Soc.* **2015**, *137*, 3638–3648.
[51] M. Aghazadeh, M. R. Ganjali, M. G. Maragheh, *Int. J. Electrochem. Sci.* **2017**, *12*, 5792–5803.
[52] M. S. Burke, L. J. Enman, A. S. Batchellor, S. Zou, S. W. Boettcher, *Chem. Mater.* **2015**, *27*, 7549–7558.
[53] J. R. S. Brownson, C. Lévy-Clément, *Phys. Status Solidi B.* **2008**, *245*, 1785–1791.
[54] NIST X-ray Photoelectron Spectroscopy Database, Version 4.1 (National Institute of Standards and Technology, Gaithersburg, 2012); http://srdata.nist.gov/xps/.
[55] U. M. Patil, R. V. Ghorpade, M. S. Nam, A. C. Nalawade, S. Lee, H. Han, S. C. Jun, *Sci. Rep.* **2016**, *6*, 35490.
[56] Y.-C. Liu, J. A. Koza, J. A. Switzer, *Electrochim. Acta* **2014**, *140*, 359–365.

© 2022 The Authors. ChemSusChem published by Wiley-VCH GmbH

[57] A. C. Garcia, T. Touzalin, C. Nieuwland, N. Perini, M. T. Koper, *Angew. Chem. Int. Ed.* **2019**, *58*, 12999–13003; *Angew. Chem.* **2019**, *131*, 13133–13137.
[58] T. ul Haq, Y. Haik, *Catal. Today* **2022**, *400–401*, 14.
[59] R. D. L. Smith, C. Pasquini, S. Loos, P. Chernev, K. Klingan, P. Kubella, M. R. Mohammadi, D. Gonzalez-Flores, H. Dau, *Nat. Commun.* **2017**, *8*, 2022.
[60] R. D. Smith, M. S. Prévot, R. D. Fagan, S. Trudel, C. P. Berlinguette, *J. Am. Chem. Soc.* **2013**, *135*, 11580–11586.
[61] R. D. L. Smith, M. S. Prévot, R. D. Fagan, S. Trudel, C. P. Berlinguette, *J. Am. Chem. Soc.* **2013**, *135*, 11580–11586.
[62] W. Xiang, N. Yang, X. Li, J. Linnemann, U. Hagemann, O. Ruediger, M. Heidelmann, T. Falk, M. Aramini, S. DeBeer, M. Muhler, K. Tschulik, T. Li, *Nat. Commun.* **2022**, *13*, 179.
[63] S. Sasidharanpillai, H. Arcis, L. Trevani, P. R. Tremaine, *J. Phys. Chem. B* **2019**, *123*, 5147–5159.
[64] E. Budiyanto, S. Salamon, Y. Wang, H. Wende, H. Tüysüz, *JACS Au* **2022**, *2*, 697–710.
[65] A. Moysiadou, S. Lee, C.-S. Hsu, H. M. Chen, X. Hu, *J. Am. Chem. Soc.* **2020**, *142*, 11901–11914.
[66] W. H. Lee, M. H. Han, Y.-J. Ko, B. K. Min, K. H. Chae, H.-S. Oh, *Nat. Commun.* **2022**, *13*, 605.
[67] C. Pasquini, L. D'Amario, I. Zaharieva, H. Dau, *J. Chem. Phys.* **2020**, *152*, 194202.
[68] M. Testa-Anta, M. A. Ramos-Docampo, M. Comesaña-Hermo, B. Rivas-Murias, V. Salgueiriño, *Nanoscale Adv.* **2019**, *1*, 2086–2103.
[69] J. M. J. Santillán, D. Muñetón Arboleda, D. F. Coral, M. B. Fernández van Raap, D. Muraca, D. C. Schinca, L. B. Scaffardi, *ChemPhysChem* **2017**, *18*, 1192–1209.
[70] Z. Lu, W. Xu, W. Zhu, Q. Yang, X. Lei, J. Liu, Y. Li, X. Sun, X. Duan, *Chem. Commun.* **2014**, *50*, 6479–6482.

Manuscript received: June 7, 2022
Revised manuscript received: July 17, 2022
Accepted manuscript online: August 3, 2022
Version of record online: September 1, 2022

© 2022 The Authors. ChemSusChem published by Wiley-VCH GmbH